

\*\*FULL TITLE\*\*  
*ASP Conference Series, Vol. \*\*VOLUME\*\*, \*\*YEAR OF PUBLICATION\*\**  
 \*\*NAMES OF EDITORS\*\*

## Turning AGN Microlensing From a Curiosity Into a Tool

C.S. Kochanek, X.Dai, C. Morgan, N. Morgan, S. Poindexter

*Department of Astronomy, The Ohio State University*

G. Chartas

*Department of Astronomy and Astrophysics, Pennsylvania State University*

**Abstract.** Microlensing of gravitationally lensed quasars by the stars in the foreground lens galaxy can be used to probe the nature of dark matter, to determine the mean stellar mass in the lens galaxy, and to measure the internal structure of quasar accretion disks. Until recently, little progress has been made toward using microlensing for these purposes because of the difficulty in obtaining the necessary data and the lack of good analysis methods. In the last few years, both problems have been solved. In particular, Bayesian analysis methods provide a general approach to measuring quantities of physical interest and their uncertainties from microlensing light curves. We discuss the data and the analysis methods and show preliminary results for all three astrophysical applications.

### 1. Introduction

Suppose I advertise to you a set of observations that simultaneously probe the nature of dark matter, the mean stellar mass in cosmologically distant galaxies, and resolves the internal structure of quasars. This sounds like a marvelous scientific opportunity. Yet despite having the capability of carrying out these observations for over a quarter of a century, there are few quantitative results.

The observations are the monitoring of gravitationally lensed quasars for the effects of microlensing by the stars in the lens galaxy. In a gravitational lens, we see (usually) two or four images of a background quasar created by the deflection of light in the gravitational field of a foreground galaxy. If we then monitor the brightness of the quasar images, we will observe them to vary due to two effects. First, if the luminosity of the quasar varies, we will see those variations in the individual images but with temporal shifts due to the different light travel times associated with each image. These time delays can be measured by cross correlating the light curves of the individual images, and they measure the surface mass density of the lens galaxy at the radius of the images from the center of the lens galaxy. Second, we will see uncorrelated variations in the brightness of the images due to *microlensing* by the stars in the lens galaxy near each image of the quasar. Our advertisement was for the scientific potential of microlensing.

Two basic problems have blocked delivering on the advertisement. The first problem is sociological. Time on optical telescopes is generally allocated by the

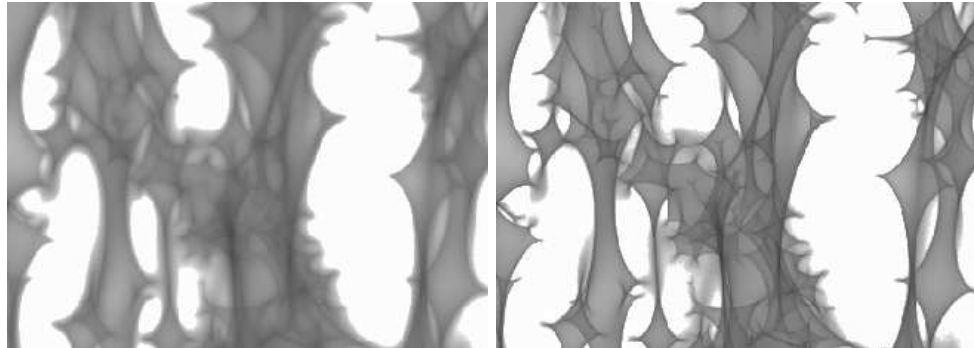


Figure 1. A typical magnification pattern for image A of Q2237+0305. The left panel is smoothed to the source size needed to fit the optical light curves. The right panel shows the same pattern for a source three times smaller. Darker regions correspond to higher magnifications. The peak magnifications drop from a factor of 10 (right panel) to a factor of 6 (left panel). The center of the lens galaxy lies to the right.

night, and this sociological choice makes it nearly impossible to monitor gravitational lenses. A scientific program to study variability in an interesting sample of lenses requires roughly 1 hour/night, *every night*, on a 1–2m class telescope. Since the time-allocation scheme does not allow for such studies, monitoring lenses has been restricted to small numbers of lenses and short periods of time. The second problem is statistical. While microlensing variability depends on the nature of dark matter, the mean stellar mass in the lens, and the internal structure of quasars, it is not amenable to simple analyses. Even for the few lenses that were successfully monitored and showed microlensing variability, there was no good way to analyze the results without making compromising assumptions.

In this brief review, we outline the physics of microlensing in §2, the nature of the data in §3, and the Bayesian Monte Carlo method we have developed to analyze the data in §4. In §5 we present results on the size of quasars, the fraction of mass in stars and the mean mass of the stars. In §6 we outline some of the physical, computational and statistical issues of our approach and how they might be addressed. In §7 we discuss the future of the method. Wambsganss (2006) provides a complete review of the microlensing field and Kochanek (2006) provides a review of strong lensing. We use a flat  $\Omega_0 = 0.3$  cosmology and a Hubble constant of  $H_0 = 100h \text{ km s}^{-1} \text{ Mpc}^{-1}$ .

## 2. The Basics Of Microlensing

The region near each lensed quasar image is characterized by three dimensionless numbers: the mean surface density  $\kappa$ , the surface density in stars  $\kappa_* \leq \kappa$  and the (tidal) shear  $\gamma$ . The surface densities are in units of the critical surface density for gravitational lensing. The surface density and the shear determine the two inverse magnification eigenvectors  $1 - \kappa \pm \gamma$ , whose values determine many of the large scale statistical properties of microlensing. The stars, or microlenses, locally deflect light rays and this leads to a complicated magnification pattern whose characteristic scale is set by the Einstein radii of the stars projected onto

the source plane

$$R_E = D_{OS} \left[ \frac{4G\langle M \rangle}{D_{OL}c^2} \frac{D_{LS}}{D_{OS}} \right]^{1/2} = (5.5 \times 10^{16}) \left[ \frac{\langle M \rangle}{M_\odot} \right]^{1/2} h^{-1} \text{cm} \quad (1)$$

where  $\langle M \rangle$  is the mean mass of the stars and we used the angular diameter distances  $D_{OL}$ ,  $D_{OS}$  and  $D_{LS}$  between the observer, lens and source for the lens PG1115+080. Fig. 1 shows some typical magnification patterns for the lens Q2237+0305. While  $R_E$  sets a scale for the features, the surface density of stars ( $\kappa_*$ ), their relative positions, and the local magnification ( $\kappa$ ,  $\gamma$ ) all interact to create complex patterns with networks of caustic curves on which the magnification is formally divergent (see Fig. 1).

These patterns are the magnifications experienced by a point source. We observe the fluctuations found by convolving the pattern with the surface brightness of the source – larger sources will show steadily smaller fluctuations. In Fig. 1 we have actually shown models convolved with a source with the typical size needed to fit the optical microlensing variability and with a source three times smaller. Quasars are extended sources with a minimum size scale of order the gravitational radius of the black holes powering quasars

$$r_g = \frac{GM_{BH}}{c^2} = (1.5 \times 10^{14}) \left( \frac{M_{BH}}{10^9 M_\odot} \right) \text{cm.} \quad (2)$$

For a standard thin accretion disk model of a quasar (Shakura & Sunyaev 1973), the black hole is surrounded by a thermally radiating disk with a temperature profile of

$$T(R)^4 = \frac{3GM_{BH}\dot{M}}{8\pi R^3\sigma} \left[ 1 - \left( \frac{R_{in}}{R} \right)^{1/2} \right] \quad (3)$$

where  $\dot{M}$  is the mass accretion rate and  $R_{in}$  is the inner edge of the accretion disk. The inner edge is in the range of  $r_g < R_{in} < 6r_g$  set by the last stable orbits for maximally rotating and non-rotating black holes. Observations of the disk at rest-frame wavelength  $\lambda$  correspond to a typical temperature  $kT_\lambda = hc/\lambda$ , so we can rewrite the leading part of the temperature scaling as  $T = T_\lambda(R_\lambda/R)^{3/4}$  where

$$R_\lambda = \frac{1}{\pi^2} \left( \frac{45}{16} \frac{\lambda^4 r_g \dot{M}}{h_p} \right)^{1/3} = (9.7 \times 10^{15}) \left( \frac{\lambda}{\mu m} \right)^{4/3} \left( \frac{M_{BH}}{10^9 M_\odot} \right)^{2/3} \left( \frac{L}{\eta L_E} \right)^{1/3} \text{cm} \quad (4)$$

and we have replaced the mass accretion rate  $\dot{M}$  by the luminosity  $L$  relative to the Eddington luminosity  $L_E$  combined with the radiative efficiency  $\eta$  of the accretion,  $L = \eta \dot{M} c^2$ . When observed face-on, the disk has a surface brightness profile of

$$f_\nu(R) = \frac{2h_p c}{\lambda^3} \left[ \exp \left( \frac{h_p c}{kT(R)\lambda} \right) - 1 \right]^{-1} = \frac{2h_p c}{\lambda^3} \left[ \exp \left( \frac{R}{R_\lambda} \right)^{3/4} - 1 \right]^{-1}, \quad (5)$$

where in the latter expression we neglect the central temperature depression of Eqn. (3) that is created by the inner edge of the disk. Numerical experiments

indicate that this approximation is safe for the moment. Thus, the scale  $R_\lambda \propto \lambda^{4/3}$  in Eqn. (4) is the characteristic size of the disk at wavelength  $\lambda$  because it is the point where the surface brightness of the disk begins to drop exponentially as the disk temperature drops below the photon energy. We may also need to worry about viewing angles, the degree to which the model breaks down very near the black hole as relativity becomes more important, and non-thermal emission (X-rays or radio).

We see fluctuations in the brightness because nothing is static. We are moving, the lens galaxy is moving, the stars in the lens galaxy are moving and the quasar is moving. Since the patterns associated with each image are different, we see microlensing as uncorrelated variations in the image fluxes. Fig. 2 shows an example of a light curve. Most studies have held the patterns fixed, ignoring the motions of the stars, and generated the fluctuations expected from a linear track across the fixed patterns. The consequences of the motions of stars have been considered theoretically (Kundic & Wambsganss 1993, Schramm et al. 1993, Wyithe et al. 2000a), and we will return to this point in §6. If we ignore the stellar motions, the bulk motions of the observer, lens and source can be reduced to a net effective velocity  $v_e$  across the magnification pattern.

One important point to understand is that observations of the lens can only measure things in “Einstein” units, where the length scale is proportional to  $R_E \propto \langle M \rangle^{1/2}$  (Eqn 1). We can convert to physical units only if we have a prior on some other quantity like the effective velocity, the mean stellar mass or the size of the quasar.

We are interested in the “physical” variables associated with the structure of the lens ( $\kappa, \kappa_*, \gamma$ ), the mass of the stars ( $\langle M \rangle$ ), the structure of the quasar ( $R_\lambda$ ) and the velocities ( $v_e$ ). We are not interested in nuisance variables such as the exact distribution of the stars or the position of the quasar on the pattern. The challenge is to analyze a set of light curves with arbitrary sampling at an assortment of wavelengths to obtain estimates of physically interesting variables.

### 3. Obtaining the Data

The major problem in collecting the data is sociological. The physical requirement is a 1-2m class telescope that routinely produces images with  $1.^{\prime\prime}0$  resolution. Data must be obtained almost every night in order to monitor large numbers of lenses varying over a broad range of time scales. There are few lenses for which we can tolerate gaps of more than 1–2 weeks during an observing season. The intrinsic variability of the quasar is generally on shorter time scales than the microlensing variability, but to remove the intrinsic variability you need to measure the time delays and correct for them. Our present program, covering about 20 lenses during the course of the year with good coverage in the R-band and sparser coverage in the J, I and B-bands, requires approximately 1 hour per night. This is largely obtained with the queue scheduled SMARTS 1.3m telescope at CTIO, with considerably less data from Northern sites like APO, FLWO and MDM.

Once you have a well-sampled light curve at one wavelength, you can use more sparsely sampled light curves at other wavelengths in order to measure the wavelength-dependence of the variability. The ability to use sparsely sampled

data at other bands is particularly important when extending the coverage to wavelengths that can only be studied with spacecraft – HST is needed to study the true ultraviolet, and Chandra is needed to study X-rays. These wavelengths are particularly interesting because they should probe regions closer to the inner edge of the accretion disk than the ground-based optical data.

#### 4. The Bayesian Monte Carlo Method

Given data  $D$ , the measured light curves, and model parameters  $p$  we can produce a model light curve and compute how well it fits the observed light curve with a  $\chi^2$  statistic to get the probability of the data given the parameters,  $P(D|p) = \exp(-\chi^2/2)$ . Using Bayes theorem and estimates of the prior probabilities  $P(p)$  for the parameters, we can estimate the probability distributions for the parameters given the data,  $P(p|D) \propto P(D|p)P(p)$ , with the usual normalizations to make the total probability equal to unity. This applies to any microlensing data we acquire.

Our basic approach is to generate random magnification patterns for a range of physical parameters ( $\kappa, \kappa_*, \gamma, \langle M \rangle$ ), convolve them with a range of randomly selected disk models ( $R_\lambda$ ), randomly generate light curves (the effective source velocity  $v_e$  and nuisance variables such as the starting point of the light curve in the pattern), compute the  $\chi^2$  values for each trial light curve and then use Bayes' theorem to combine all the results for the individual trials in order to determine the probability distributions for the physical parameters – essentially we do the integrals needed for the Bayesian analysis as a large Monte Carlo integral. The only surprise about the approach is that such a brute force method can successfully generate significant numbers of model light curves that are statistically acceptable fits to the observed light curves.

Everything we can measure from a microlensing light curve will be in “Einstein” units where lengths scale as  $\langle M \rangle^{1/2}$ . In order to convert from Einstein units to physical units, we require a prior on some variable with dimensions. Our three possible choices are the mean mass itself,  $\langle M \rangle$ , the effective velocity  $v_e$ , and the accretion disk size,  $R_\lambda$ . Each of these variables has a reasonable physical prior. We know the mean stellar mass in our galaxy is (generously) in the range  $0.1M_\odot < \langle M \rangle < 1.0M_\odot$ , and this is a good choice for the prior because the uncertainty in the length scale depends only on the square root of the mass scale. If we assume an accretion disk model, then we can define a prior for the size of the accretion disk because the observed flux of the quasar determines the disk size if we understand the structure and emission mechanism of the disk. For example, in a standard thin disk with no inner edge,

$$R_\lambda \simeq \frac{1.2 \times 10^{15}}{\sqrt{\cos i}} \left( \frac{H_0 D_{OS}}{c} \right) \left( \frac{\lambda_{obs}}{\mu\text{m}} \right)^{3/2} 10^{-0.2(I-19)} h^{-1} \text{cm} \quad (6)$$

where  $I$  is the (magnification corrected) I-band magnitude of the quasar and  $i$  is the disk inclination angle. In many ways, however,  $\langle M \rangle$  and  $R_\lambda$  are the most interesting physical variables in the problem, so it would be better to assume very broad (or no) priors for these variables.

The last possibility is the effective velocity, which depends on our motion, the peculiar velocity of the lens and quasar host galaxies, and the local velocities

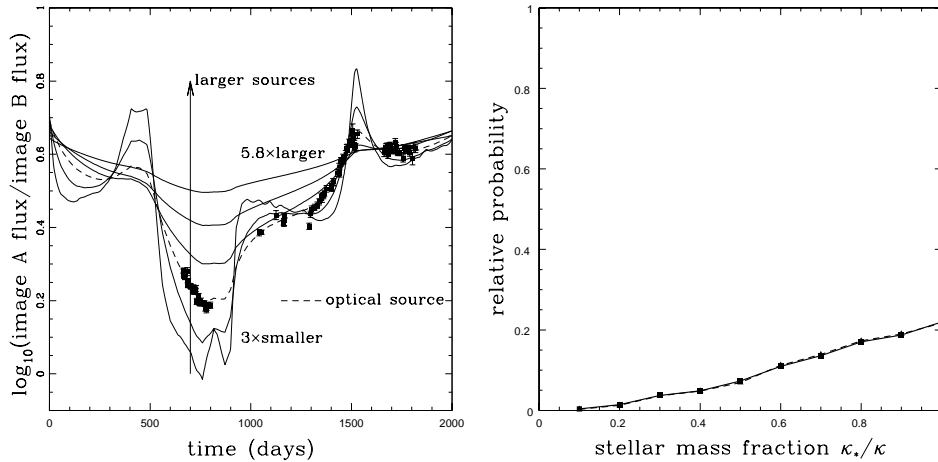


Figure 2. Model light curves for Q2237+0305. The dashed curve is a light curve generated by the Bayesian analysis that fit the OGLE V-band data (points) well and is then extrapolated across the magnification pattern. The solid lines show the effects of changing the source size by 0.25 dex (a factor of 1.7) per curve. Larger sources more heavily smooth the magnification pattern and show less variability, and vice versa for small sources. For a  $T \propto R^{-3/4}$  disk, the K-band and 2500Å sources should be roughly 5 times larger/smaller than the optical source (i.e. three steps from the dashed curve).

Figure 3. The fraction of the surface density of Q2237+0305 in stars,  $\kappa_*/\kappa$ , based on the full OGLE light curves. The likelihood for  $\kappa_*/\kappa \sim 1$  has increased markedly compared to our original result in Kochanek (2004) with the addition of the OGLE-III light curve data. Unlike the typical gravitational lens, where we expect  $\kappa_*/\kappa \sim 0.1\text{--}0.2$ , Q2237+0305 should have  $\kappa_*/\kappa \sim 1$  because we see the quasar images through the bulge of a low redshift spiral galaxy.

of the stars in the lens galaxy. We know our motion well because it is simply the projection of the CMB dipole velocity onto the source plane of the lens. For most lens galaxies, we know the local velocity dispersion of the stars reasonably well either from the image separations in the lens or by direct measurement. Ideally we include this directly by allowing the stars to move, but it can be mimicked statistically (Wyithe et al. 2000a). The biggest uncertainties are the unknown transverse peculiar velocities of the lens and quasar host galaxies, with the former being the most important because peculiar velocities grow with time. Here we must use a statistical model based on N-body simulations of structure formation, possibly modified when we know that the lens is in a group or cluster and should have a higher than random peculiar velocity.

## 5. Preliminary Results

We have just reached the point where our observations of microlensing in a large number of lenses and a over range of wavelengths have started to produce results. Here we present some examples of estimating the stellar mass fraction,

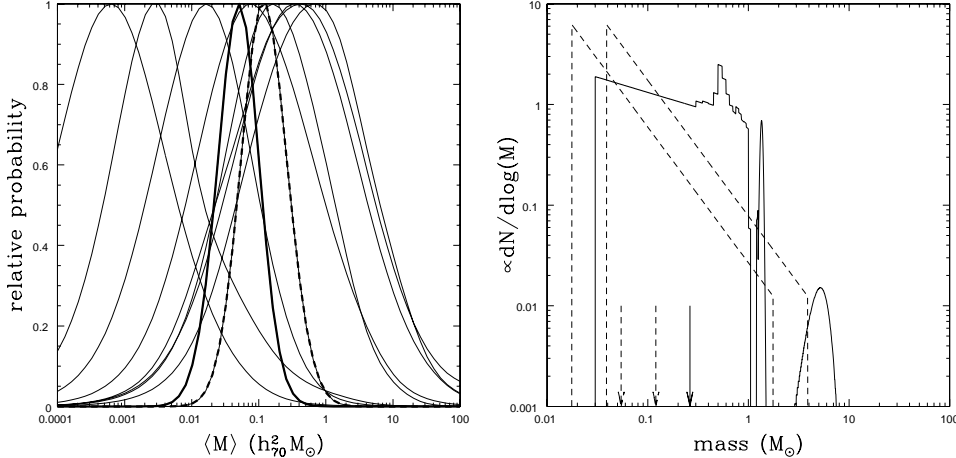


Figure 4. The mean mass  $\langle M \rangle$  of the microlenses for 8 systems (light curves) and the joint probability (heavy solid curve). The heavy dashed curve shows the effect of dropping the two systems favoring the lowest masses. Dropping the two systems favoring the highest masses leads to a similar shift, but towards lower masses. The uncertainties in the results for the individual systems are roughly equally due to the model (prior) for the physical velocities and the uncertainties in the effective velocities from fitting the data.

Figure 5. A comparison of our model mass functions (dashed lines) to a realistic mass function for the Galactic disk (solid curve) by Gould (2000). The arrows show the mean masses for the three mass functions, and the two microlensing mass functions correspond to the two cases shown in Fig. 4. The three peaks in the Gould (2000) mass function correspond to white dwarfs, neutron stars and black holes. Theoretical studies of microlensing strongly suggest that our estimates are not sensitive to the shape of the mass function, but this comparison suggests that we should shift to a flatter mass function than the Salpeter form typically used in microlensing calculations to allow for cleaner comparisons.

the mean stellar mass and the structure of quasars as a function of black hole mass and wavelength. Let us start with an example of the data, in this case, a published V-band light curve of the Q2237+0305 image A/B flux ratio by the OGLE collaboration (Wozniak et al. 2000). We used the OGLE data on this system in Kochanek (2004) to develop the analysis method and to demonstrate its power as a means of analyzing microlensing data. Fig. 2 shows the original light curve we analyzed and one of the well-fitting model light curves produced by the Bayesian Monte Carlo analysis. To illustrate the sensitivity of light curves to source size, we also show the expected light curves for sources of a different size from the V-band wavelength used by OGLE.

One interesting application of the Q2237+0305 microlensing data is shown in Fig. 3, where we estimate the fraction  $\kappa_*/\kappa$  of the surface density near the quasar images that is composed of stars. This is one of the more difficult variables to measure from microlensing data when the source size is also unknown, but the result is steadily converging to the expected result for Q2237+0305 of

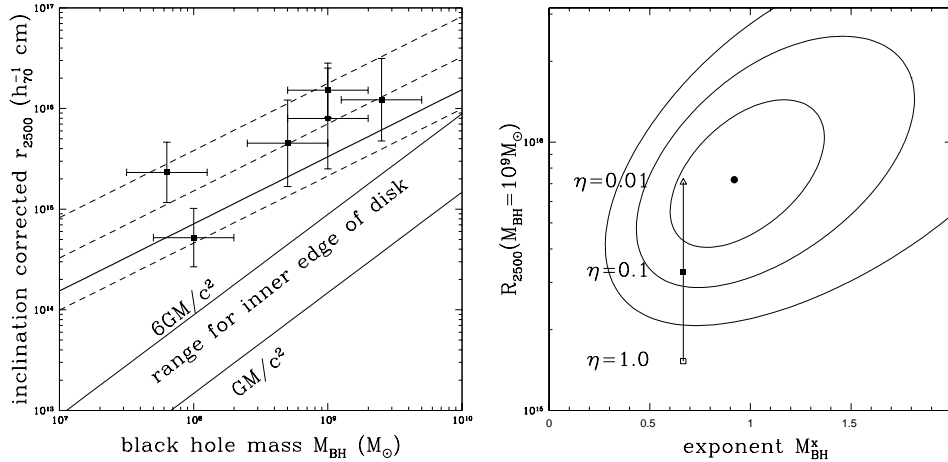


Figure 6. (Left) Accretion disk size versus black hole mass at 2500Å in the rest frame of the quasar assuming the mean disk inclination. This roughly corresponds to our standard R-band monitoring filter. The expectation for a standard thin disk and a quasar radiating at the Eddington limit with an efficiency of  $\eta = 0.1$  is shown by the heavy solid line. The dashed lines show the expected sizes for a  $z = 1.5$  quasar at the K (top), H and B-bands to illustrate the expected dependence on wavelength. Remember that size ratios can be more accurately measured than absolute sizes. The lines at  $r_g = GM_{BH}/c^2$  to  $6r_g$  show the expected range for the inner edge of the accretion disk.

Figure 7. (Right) A power-law fit to the accretion disk size as a function of black hole mass in Fig. 6. The contours show the 1-3 $\sigma$  limits on the two variables. The points connected by the vertical line show the expectation for thin disk models radiating at Eddington with efficiencies of  $\eta = 0.01$ ,  $0.1$  and  $1.0$ . The estimates from the microlensing data are mildly consistent with the theoretical model unless the radiative efficiency is very low.

$\kappa_*/\kappa \simeq 1$ . We know the “correct” answer in this case because the lens is the bulge of a low redshift spiral galaxy where we expect a negligible contribution to the total surface density from dark matter.

We can also take a preliminary look at the mean mass of the microlenses  $\langle M \rangle$ . The mass is difficult to measure for any individual lens because it depends on the square of the velocity,  $\langle M \rangle \propto v_e^2$  and we have only statistical information on the peculiar velocities of the lens. As a result, we can probably never do better than a factor of  $\sim 4$  uncertainty for  $\langle M \rangle$  in any one lens. With ensembles of lenses, however, we can average out the uncertainties due to the peculiar velocities, to produce an accurate estimate. Fig. 4 shows a preliminary attempt at this, where we have averaged over the mass estimates for eight lenses. Formally, the median mass estimate is  $0.05M_\odot$  with a 95.4% confidence region of  $0.01M_\odot < \langle M \rangle < 0.21M_\odot$ . The result is relatively robust. For example if we drop the two lenses favoring the lowest masses, the median rises to  $0.12M_\odot$  with  $0.02M_\odot < \langle M \rangle < 0.62M_\odot$  at 95.4% confidence. Such masses may be mildly inconsistent with local estimates of the mass function, as shown in Fig. 5, where

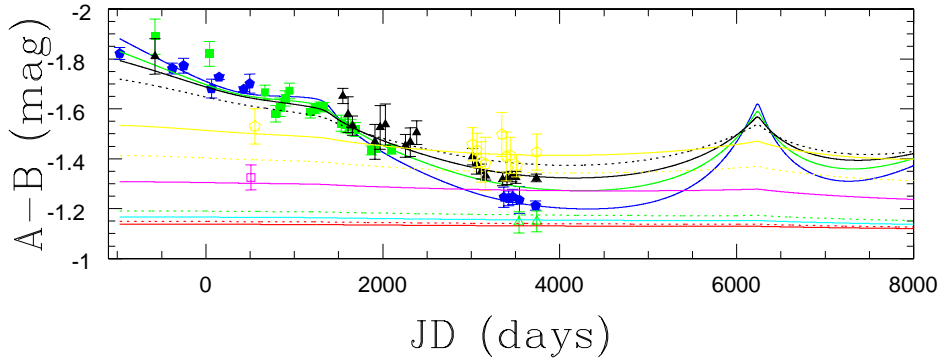


Figure 8. The HE1104–1805 light curves. The curves show a model for the BVRIJHK and IRAC Channel 1 ( $3.6\mu\text{m}$ ) to 4 ( $8\mu\text{m}$ ) flux ratios with B-band at the top and  $8\mu\text{m}$  on the bottom at the beginning of the time series. The points are 90-day running averages of the B (pentagon), V (square), R (triangle), J (open pentagon), K (open square) and  $3.6\mu\text{m}$  (open triangle) flux ratio measurements. The I-band, H-band, the other IRAC channel data are not shown (but are consistent with the model), and only points on the running average separated by at least 45 days are plotted. Note the optical color reversal between the early periods and the present epoch. The uncertainties in the disk structure estimate shown in Fig. 10 are driven by the lack of near-IR data the two anomalous V-band data points in the early phases. The history includes data from Remy et al. (1998), Gil-Merino et al. (2002), Ofek & Maoz (1993) Schechter et al. (2003) and Wyrzykowski et al. (2003) as well as our own data.

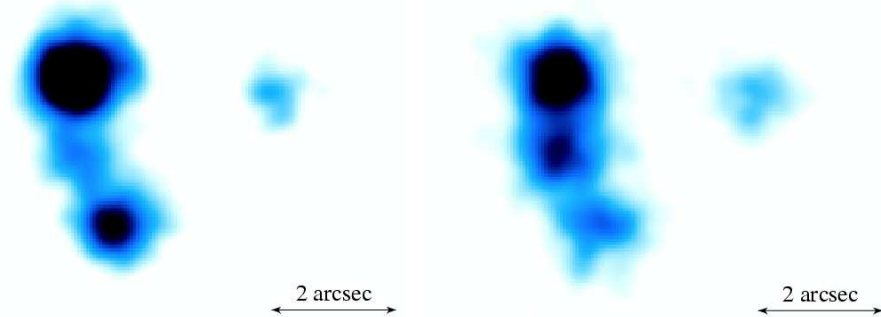


Figure 9. Two epochs of X-ray data for RXJ1131–1231. The left panel is the Blackburne et al. (2006) data from 12 April 2004, and the right panel is our 10 March 2006 image. Notice the dramatic changes in the A-C X-ray flux ratios produced by microlensing. The optical flux ratios are very different for both epochs.

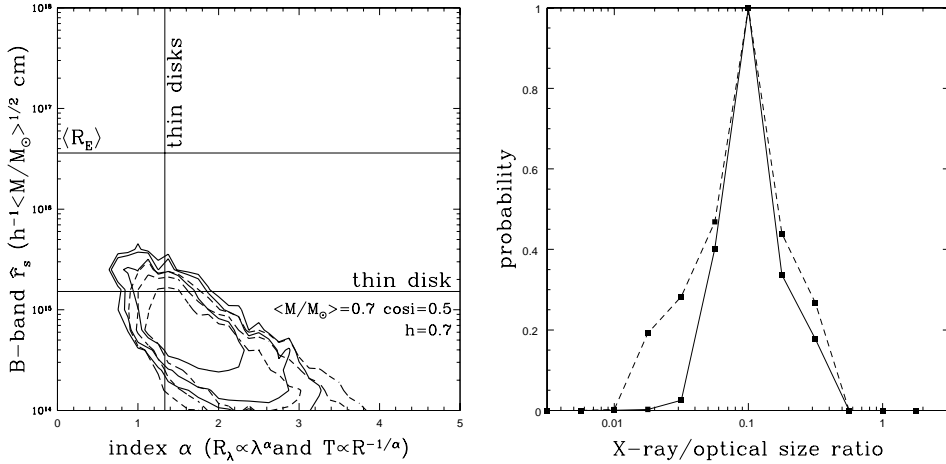


Figure 10. (Left) Likelihood contours for the scaling of the HE1104-1805 disk size with wavelength. The contours are drawn at the 68%, 90% and 95% enclosed likelihood contours for either a constant (solid) or logarithmic (dashed) prior on the disk size. The lines indicate the mean Einstein radius  $\langle R_E \rangle$ , the expected B-band disk size based on the Peng et al. (2006) estimate that  $\log(M_{BH}/M_\odot) = 9.4$ , and the expected exponent  $\alpha = 4/3$  for the scaling of the size with wavelength,  $R_\lambda \propto \lambda^{4/3}$ .

Figure 11. (Right) The probability distributions for the ratio of the X-ray and optical source sizes using either the first (dash) or both (solid) X-ray observations of RXJ1131. Note that the results are consistent, and that the error bars shrink with the addition of more data. The formal uncertainties are approximately a factor of 1.7 ( $\pm 0.23$  dex) using both epochs. These preliminary results assumed an SIE model for the lens which does not agree with the measured time delays of the lens.

we compare our Salpeter mass functions with these two normalizations to a detailed model for the mass function of the Galactic disk from Gould (2000). That the shapes differ is not important, as there are extensive microlensing simulations demonstrating that only the mean mass of the microlenses is easily measured (e.g. Paczyński 1986, Wyithe et al. 2000b), although we should probably shift to a shallower mass function just to simplify comparisons. The important point is that our estimates of the mean mass are significantly lower than the  $\langle M \rangle = 0.26M_\odot$  of the Galactic model. On the other hand, the low mass cutoff at  $0.03M_\odot$  in the Galactic model is somewhat arbitrary.

We now have enough well-sampled light curves that measurements of disk sizes are becoming routine. Fig. 6 shows a preliminary correlation of disk size with black hole mass  $M_{BH}$ . The results track the expectations for thin disk theory from §2 over two decades in black hole mass, where the black hole mass estimates from Peng et al. (2006) are based on the emission line widths of the quasars. A formal fit to the estimates is marginally inconsistent with thin disk theory, finding a slope of  $R_\lambda \propto M_{BH}^x$  that is somewhat steeper than the predicted 2/3 (Eqn. 4) and a higher normalization than expected for accretion at the Eddington limit with an efficiency  $\eta > 0.1$ . A potentially more serious

problem, also noted by Pooley et al. (2006), is that the disk sizes are larger than the sizes predicted by matching a black body emitting disk to the observed I-band magnitudes (Eqn. 6), even though the microlensing and black body size estimates are proportional to each other. The origin of this discrepancy is probably due to a conspiracy of several smaller factors such as contamination of the light curves by emission from larger scale sources like the quasar broad lines, radiation transfer problems in the disk atmosphere like line blanketing, scattering and reradiation of the disk emission, and differences in the advection of energy or the structure of real disks from the thin disk model. Only the latter two possibilities represent genuine changes from a thin disk.

One way to attack these problems of disk structure is to measure disk sizes as a function of wavelength. Fig. 8 shows the wavelength-dependent changes in the flux ratio of the two-image lens HE1104–1805, and Fig. 9 shows the dramatic variations in the X-ray flux ratios of the lens RXJ 1131–1231. Size ratios can be measured more accurately than absolute sizes because the ratios depend only on the relative variability amplitudes. Image A of HE1104–1805 has slowly switched from being bluer than image B to being redder in the optical/near-infrared while the mid-infrared fluxes agree with the flux ratio of the broad emission lines (e.g. Wisotzki et al. 1995). An unexpected feature of the wavelength ordering, although one which we had no difficulty reproducing, is the present situation where A is brightest relative to B in the J band and becomes relatively fainter at both bluer and redder wavelengths. If we fit these light curves with a model in which the size of the disk is a power-law referenced to the size in the B-band,  $R_\lambda = R_B(\lambda/\lambda_B)^\alpha$ , we find the likelihood distributions shown in Fig. 10. The results are consistent with the expectations of thin disk theory given the estimated black hole mass from Peng et al. (2006), but the exact results depend on the prior adopted for the source size. The incomplete convergence is probably due to the very limited data in the redder bands in the early phases of the light curves.

We can also estimate the size ratio between the X-ray emitting regions and the optical disk by simultaneously fitting the optical light curve and sparse X-ray measurements. Fig. 11 shows that the X-ray source in RXJ 1131–1231 is roughly an order of magnitude more compact than the optical source, with remarkably small uncertainties given that the estimate is based on only two X-ray observations. If X-ray emission comes from near the last stable orbit of the black hole, as our estimates so far have suggested, then we should see a large optical/X-ray size ratio in a system like RXJ1131–1231 with a relatively low mass black hole ( $M_{BH} \simeq 10^{7.8} M_\odot$ ) and a smaller size ratio in a system like Q2237+030 with a relatively high mass black hole ( $M_{BH} \simeq 10^{9.0} M_\odot$ ) because the disks of lower mass black holes are hotter and the observed-frame optical emission comes from farther out in the disk (see Fig. 6). A preliminary analysis of our X-ray observations of Q2237+030 agrees with this expectation.

## 6. Physical, Computational and Statistical Issues

In this section we discuss aspects of the physical models, the computational methods and the statistical analysis that need to be considered. Generally,

they are not independent – physical issues may arise because of computational limitations and so forth.

### 6.1. Physical Issues

We are principally worried about four physical issues in the way we analyze the problem, which we discuss in order from very mildly worried to more seriously worried. We have experimented with most of the issues, and for the moment they appear not to be a limiting problem compared to the difficulty in obtaining the data, but this will change as the data improves.

First, in our standard models we assume a Salpeter mass function with a dynamic range of a factor of 100 in the mass. We have experimented with smaller mass ranges or even single masses, and we have been unable to distinguish between mass functions or find significant differences in the results for other variables from changes in the mass functions. This experience matches that from extensive theoretical studies of the effect of the mass function over the last 20 years (e.g. Wyithe et al. 2000b). Reasonable mass functions have most of the mass in a limited range, and the physical scales depend only on the square root of the mass, so this insensitivity is not surprising particularly given the significant uncertainties in results based on the available data. Eventually, however, it may matter.

Second, we can choose to fit only the time variations in the image flux ratios that are the easily observed signature of microlensing, or to also fit the actual flux ratios. If you examine the magnification patterns in Fig. 1, you see that the pattern is typically divided into broad, relatively smooth regions of demagnification separated by narrow regions of higher magnification consisting of dense networks of caustics. A given amplitude of variability can be created by moving slowly through a region of high magnification with a large source or by moving rapidly through a region of low magnification with a smaller source. Any information that constrains you to a particular region of the maps can greatly reduce degeneracies in the solutions.

Forcing the models to match the flux ratios predicted by the “macro” model for the overall mass distribution is such a constraint. The “macro” model is already part of the microlensing model because it is the source of the estimated values of the surface density  $\kappa$  and shear  $\gamma$  near each image used in generating the patterns. There are two problems with forcing the models to match the observed flux ratios. One problem is that undetected satellite galaxies (“substructures”) near the lensed images can change the image magnifications while having little other detectable effect, so it is risky to force the flux ratios to match that of a standard “macro” model (e.g. Kochanek & Dalal 2004). These satellites may also mean that the estimates of  $\kappa$  and  $\gamma$  used to generate the magnification maps are sometimes incorrect. A second problem is that the observed flux ratios, but probably not their time variations, can be affected by absorption in the interstellar medium of the lens galaxy (e.g. Falco et al. 1999). In short, adding the absolute flux ratios as a constraint would be very useful, but requires a clear understanding of these other systematic problems.

Third, our current disk model is a face-on thin disk without the central temperature depression created by the inner edge of the accretion disk (Eqns. 3-5). At fixed wavelength, neglecting the inner edge has considerably less consequence

than one might naively expect – at fixed wavelength little flux is radiated there and the finite resolution of the magnification patterns eliminates the formal surface brightness divergence in Eqn. (5). We have experimented with adding the hole or simply using a Gaussian and we cannot statistically distinguish the models with the present data. This is again the expectation from earlier theoretical work – microlensing is primarily sensitive to an effective smoothing area, and the resulting size estimate is only weakly sensitive to the true surface brightness profile (e.g. Mortenson et al. 2005). Once we can distinguish profiles, our problems begin, because the space of models increases dramatically once we move away from this simple model. Even within the context of the standard thin disk, there is the scale of the inner disk edge ( $R_{in}$ ) and the disk inclination. For more complex disk models, there are relativistic corrections to the observed temperatures and photon trajectories, effects from variable scale heights coupled with the viewing angle, more realistic radiation transfer out of the disk, non-thermal emission mechanisms, and the inner disk may be a thick torus rather than a standard thin disk (e.g. Li et al. 2005).

While distinguishing different spatial structures for the disk simply by fitting the light curve measured in a single band, determining the structure of the disk as a function of wavelength is relatively straight forward. Smaller sources have larger variability amplitudes than bigger sources, so the signature of size changes is unambiguous. Additionally, ratios of source sizes are dimensionless quantities that are unaffected by uncertainties in the mass scale  $\langle M \rangle$ , so we can determine size ratios more accurately than the absolute size scale. The changes in size over the optical/near-IR wavelength baseline are quite large – if  $R_\lambda \propto \lambda^{4/3}$  (Eqn. 4), the disk size changes by a factor of 3.4 over our J-band to B-band wavelength baseline, which corresponds to over an order of magnitude change in the area of the source.

Finally, the issue we are most concerned about is the use of a static magnification pattern where the stars do not move. The concern is not that we are getting incorrect results, but that the compromises from using static patterns force us to results with broader uncertainties than we would have if we allowed dynamic patterns. We are forced to this approximation by computational issues – as we discuss in §6.2.

If you examine the maps in Fig. 1, you can see that the maps have different scales in the strongly and weakly sheared directions, so the velocity required to produce a given amount of variability depends on the direction of the motion. The source velocity vector is the same for all images, so we should see different statistics for the variability of the images depending on the angle between the source velocity and the strongly sheared direction of the magnification patterns. If we use a fixed pattern and have no random stellar motions, it is unreasonable to force a fixed source velocity – instead, we use a fixed velocity magnitude but allow the direction on each pattern to be random. Another problem with fixed patterns is that we lose the contribution of “pattern velocities” created by rearrangements of the caustics as the stars move. Pattern velocities can be very much higher than physical velocities, and may be the source of the rapid microlensing variability observed in HE1104–1805 (Schechter et al. 2003).

## 6.2. Computational Issues

There are three general computational issues: (1) building magnification maps, (2) fitting them into computer memory, and (3) rapidly generating the results for trial light curves.

We generate the magnification maps by “shooting” a uniform grid of light rays through a star field, bending the trajectory based on the gravitational fields of the stars and then counting where the rays land on the source plane (Kayser et al. 1986, Schneider & Weiss 1988). The magnification at point on the source plane is the ratio between the input ray density and the density of rays reaching that point on the source plane. The problem is that stars, as point masses, have divergent ray deflections at small impact parameters, so stars very distant in projection from a point in the magnification map may contribute to the result. Traditionally the solution has been to populate a large region with stars in order to determine the source magnification maps for a much smaller region. This is relatively inefficient, and it leads to magnification maps with edges that make it difficult to generate random light curves because you would have to avoid any edge-crossing path. We solve this problem by using source and lens plane regions both of which are periodic and correspond to projections of each other. In essence, we shoot the rays through an infinite, if periodic, star field, and the resulting magnification patterns have no edges. In order to make both the lens and source planes periodic, we must adjust the desired shear  $\gamma$  by an amount of order the inverse of the array dimensions ( $< 10^{-3}$ ), but this is a small enough to have no physical consequences.

The next problem is memory. The magnification maps must have a large enough outer scale to be statistically representative of the star field and to allow the production of large numbers of independent light curves. They must also have a small enough pixel scale to resolve the gravitational radius of the quasar black hole. Typically a  $4096^2$  grid scale is adequate to cover a region with an outer scale of  $20\text{-}40R_E$  and an inner scale that resolves the disk. A single  $4096^2$  magnification pattern is only 67 MByte, or 268 Mbyte for four images. For a single light curve, this is all that is necessary because models for different source sizes can be run independently. For models with multiple light curves, each requiring a different source size, the convolved patterns for all source sizes must be in memory – a four-image lens with 10 source sizes (2.7 GByte) will fit on a standard computer, but it is beginning to push the limits. The big problems arise when we allow the stars to move and we need an animated sequence of magnification patterns. This can easily require 100 independent magnification patterns for each image. Add multiple source sizes, and the memory requirements quickly approach several hundred Gbytes. The present version of the code is multi-threaded, so such large problems can be run efficiently on shared-memory supercomputers, but it is not parallelized, so it cannot be run on clusters. Parallelization may not be effective because we must do random look-up of points in magnification maps spread across the processors.

The remaining computational issue is simply that of speed when faced with performing the necessary Bayesian integrals over all the nuisance and physically interesting variables. We use several tricks to rapidly find regions producing good fits to the data, and these raise some of the statistical issues discussed in the next section. Our first trick is to only use trial light curves that fit the

data better than a threshold  $\chi^2$ , usually a few times the number of degrees of freedom  $N_{dof}$ , in the Bayesian integrals. The advantage of doing this is that rather than fitting the whole light curve we fit it as a sequence of randomly ordered points and then discard the trial if the goodness of fit ever exceeds the threshold. This leads to an enormous gain in execution speed because many trials are thrown away after fitting a very small number of points. To minimize biases, we periodically generate new random orderings of the light curve. The second trick is that for light curves that pass the threshold we optimize the initial position of the source, the direction of motion and allow for small fractional changes in the velocity. Only small changes in the velocity are allowed because we want the velocity to change by significantly less than the scales on which we will eventually bin the velocities for later analysis. Essentially, we have a hidden, localized maximum likelihood loop for the nuisance variables.

### 6.3. Statistical Issues

As we have currently implemented the code, there are several lingering statistical issues.

We start with a  $\chi^2$  statistic as our estimate for the probability that a particular trial light curve  $i$  fit the data,  $P(D|p) = \exp(-\chi_i^2/2)$ . When we have a light curve with significant numbers of data points, the resulting probabilities are very sensitive to whether we have correctly estimated the uncertainties, systematic as well as statistical, in the light curves. Small changes in the estimated uncertainties dramatically reweight the probabilities. We deal with this uncertainty by assuming that the photometric errors themselves have some uncertainties, characterized by another nuisance parameter, and then averaging the probabilities over a range for this variable.

For the computational reasons outlined above, we have used fixed magnification patterns in our current analyses rather than allowing the stars to move. We compensate for this simplification in two ways. First, we allow the direction of motion to be a random independent variable *for each image*. This is clearly incorrect for the bulk velocities, but it should fail in a statistically conservative manner by producing broader probability distributions. It should, however, partly mimic the effects of random motions of the stars. Second, in the prior for the effective velocity we must somehow mimic the effect of the random velocities of the stars. A random bulk velocity, like the peculiar velocity of the lens galaxy, has a non-trivial probability of values much smaller than the rms peculiar velocity. Similarly, each star in the pattern has a non-trivial probability of having a velocity that is small compared to the velocity dispersion of the lens. The star field creating the magnification pattern includes the effects of many stars and so the “statistical” velocities of the stars creating the pattern are unlikely to differ significantly from the velocity dispersion of the stars. We can mimic this physical effect statistically, but it will introduce some biases (Wyithe et al. 2000a) that should be small compared to our present uncertainties.

The trick introduced to speed up the calculations means that we have cheated slightly in doing the Bayesian Monte Carlo integrals. When we drop a trial because it does not reach the  $\chi^2$  threshold, it is lost forever because we never calculate its true goodness of fit. While the probability associated with such light curves  $P(D|p) = \exp(-\chi^2/2)$  is negligible compared to one producing a good fit,

they make a contribution to the Bayesian integrals of  $n(\chi^2) \exp(-\chi^2/2)$  which is the low probability multiplied by the number of such trials  $n(\chi^2)$ . We need to be sure that this total contribution of poorly fitting trials still has no statistical weight in the Bayesian integrals. Experiments with adjusting the threshold indicates that this is not an important issue.

The inner optimization loop is the last issue. Essentially, we take a small volume in a sub-space of the parameters and adopt the localized maximum likelihood solution rather than the full Bayesian integral over that sub-space. A better way of performing this step would be to also calculate a statistical weight for the volume sampled by the optimization, or to approximate this from the curvature of the  $\chi^2$  near the maximum (i.e. a local Laplace approximation). That being said, we have not seen any difference in the results from using this procedure versus dropping the local optimization.

## 7. Summary

We have reached the point where we can begin to use microlensing as an industrial tool. The data allows us to study problems – stellar mass fractions, mean stellar masses and quasar structure – that are virtually impossible to probe with other methods. Our main bottleneck now is time. Time matters on two levels. The first issue is simply observing time. We have enough to monitor approximately 20 lenses well at one wavelength (R-band), and to obtain sparse coverage at other wavelengths (J,I,V and B-bands) and occasional data from HST and Chandra at X-ray and UV wavelengths blocked by the atmosphere. The second issue is that the characteristic time scales for microlensing are long – roughly a decade for any particular image. For good statistical results we need to accumulate “image monitoring centuries” either by monitoring many lenses for shorter periods of time or a few lenses for very long periods of time. Given that all the results to date are being obtained with roughly 10% of the time on a 1.3m telescope, there is enormous room to accelerate the scientific program. All it requires is a few more queue-scheduled telescopes, hopefully in the 2-meter class.

Some of the most interesting problems require greater use of HST and Chandra because we expect the UV and X-ray emission of the accretion disk to come from the regions closest to the black hole. In particular, the microlensing of wavelengths shortward of the 3500Å atmospheric cutoff should show significant differences between the lower mass systems ( $M_{BH} \sim 10^8 M_\odot$ ) and the high mass systems ( $M_{BH} \sim 10^9 M_\odot$ ) because they correspond to regions still well outside the inner edge of the disk for the low mass systems but to regions very close to the inner edge for the high mass systems (see Fig. 6). The X-ray observations need to be extended from short observations sufficient to measure broad band variability, to long observations where we can examine the microlensing of the X-ray spectrum, particularly the Iron K $\alpha$  lines. Existing data show evidence for microlensing of the lines relative to the continuum (e.g. Dai et al. 2003), but better data is required to produce clean results.

**Acknowledgments.** The authors would like to thank G. Garmire for using some of his guaranteed CXO time to make some of these observations, and M. Dietrich, P. Osmer, B. Peterson, and R. Pogge for extensive discussions about

quasar structure. This work is based on observations made with the Spitzer Space Telescope, which is operated by the Jet Propulsion Laboratory, California Institute of Technology under a contract with NASA. Support for this work was provided by NASA through Cycle 2 award 20451 issued by JPL/Caltech. Support for this work was provided by the National Aeronautics and Space Administration through Chandra Award Number 6836 issued by the Chandra X-ray Observatory Center, which is operated by the Smithsonian Astrophysical Observatory for and on behalf of the National Aeronautics Space Administration under contract NAS8-03060.”

## References

Blackburne, J.A., Pooley, D., & Rappaport, S., 2006, *ApJ*, 640, 569  
 Dai, X., Chartas, G., Agol, E., Bautz, M.W., & Garmire, G.P., 2003, *ApJ*, 589, 100  
 Falco, E.E., Impey, C.D., Kochanek, C.S., Lehár, J., McLeod, B.A., Rix, H.-W., Keeton, C.R., Muñoz, J.A. & Peng, C.Y., 1999, *ApJ*, 523, 617  
 Gil-Merino, R., Wisotzki, L., & Wambsganss, J., 2002, *A&A*, 381, 428  
 Gould, A., 2000, *ApJ*, 535, 928  
 Kayser, R., Refsdall, S., & Stabell, R., 1986, *A&A*, 166, 36  
 Kochanek C.S., 2004, *ApJ*, 605, 58  
 Kochanek, C.S., 2006, in *Gravitational Lensing: Strong Weak and Micro*, Saas-Fee Advanced Course 33, G. Meylan, P. North, P. Jetzer, eds., (Springer: Berlin) 91 [astro-ph/0407232]  
 Kochanek C.S. & Dalal, N., 2004, *ApJ*, 610, 69  
 Kudnic, T., & Wambsganss, J., 1993, *ApJ*, 404, 455  
 Li, L.-X., Zimmerman, E.R., Narayan, R., & McClintock, J.E., 2005, *ApJS* 157, 355  
 Mortonson, M.J., Schechter, P.L., & Wambsganss, J., 2005, *ApJ*, 628, 594  
 Ofek, E.O., & Maoz, D., 2003, *ApJ*, 594, 101  
 Paczyński, B., 1986, *ApJ*, 301, 503  
 Peng, C.Y., Impey, C.D., Rix, H.-W., Kochanek, C.S., Keeton, C.R., Falco, E.E., Lehár, J., & McLeod, B.A., 2006 *ApJ* in press [astro-ph/0603248]  
 Pooley, D., Blackburne, J.A., Rappaport, S., & Schechter, P.L., 2006, *ApJ* submitted [astro-ph/0607655]  
 Remy, M., Claeskens, J.-F., Surdej, J., Hjorth, J., Refsdal, S., Wucknitz, O., Sorensen, A.N., & Grundahl, F., 1998, *NewA*, 3, 379  
 Schechter, P.L., Udalski, A., Szymanski, M., Kubiak, M., Pietrzynski, G., Soszynski, I., Woźniak, P., Zebrun, K., Szewczyk, O., & Wyrzykowski, L., 2003, *ApJ*, 584, 657  
 Schneider, P., & Weiss, A., 1988, *ApJ*, 330, 1  
 Schramm, T., Kayser, R., Chang, K., Nieser, L., & Refsdal, S., 1993, *A&A*, 268, 350  
 Shakura, N.I., & Sunyaev, R.A., 1973, *A&A*, 24, 337  
 Schechter, P.L., et al., 2003, *ApJ*, 584, 657  
 Wambsganss, J., 2006, in *Gravitational Lensing: Strong Weak and Micro*, Saas-Fee Advanced Course 33, G. Meylan, P. North, P. Jetzer, eds., (Springer: Berlin) 453 [astro-ph/0604278]  
 Wisotzki, L., Koehler, T., Ikonomou, M., & Reimers, D., 1995, *A&A*, 297  
 Wozniak, P.R., Alard, C., Udalski, A., Szymanski, M., Kubiak, M., Pietrzynski, G., Soszynski, I. & Zebrun, K., 2000 *ApJ*, 529, 88  
 Wyrzykowski, L., et al., 2002, *AcA*, 53, 229  
 Wyithe, J.S.B., Webster, R.L., & Turner, E.L., 2000a, *MNRAS*, 312, 843  
 Wyithe, J.S.B., Webster, R.L., & Turner, E.L., 2000b, *MNRAS*, 315, 51